

https://dspace.org/

Experimental study and neural networkbased prediction of thermal performance of applying baffles and nanofluid in the doublepipe heat exchangers

A Khadang; Mousa Nazari; Heydar Maddah; M H Ahmadi; Mohsen Sharifpur

https://hdl.handle.net/10539/40364
WOS

Downloaded from a DSpace repository. https://dspace.org/

Journal of Thermal Analysis and Calorimetry (2024) 149:4239–4259
https://doi.org/10.1007/s10973-024-12969-0

Experimental study and neural network-based prediction of thermal performance of applying baffles and nanofluid in the double-pipe heat exchangers

Amirhossein Khadang[1] · Mousa Nazari[2] · Heydar Maddah[3,4] · Mohammad Hossein Ahmadi[5] · Mohsen Sharifpur[6,7,8]

Received: 17 December 2023 / Accepted: 27 January 2024 / Published online: 16 March 2024
© Akadémiai Kiadó, Budapest, Hungary 2024

Abstract

The present study's goal was to investigate the efficiency of applying carbon/water Nanofluid and triangular baffles in the double-tube heat exchangers. The Reynolds number was in the range of 4000 to 14,000, and the carbon/water Nanofluid, which was with various volume fractions ranged between 0.1 and 0.3 volume percentages, was applied. Moreover, triangular baffles were implemented as turbulators with the numbers of 4, 8, and 12, as well as angles of 70° and 40°. Using the response surface method, the experiments design was carried out. The prediction process was eventually conducted using Perceptron artificial neural network that included the input data of Reynolds number, Nanofluids volume fraction, baffles number and angle, as well as Nusselt number target. Results showed that the simultaneous use of 12 triangular baffles at the 40° angle and a Nanofluid with a 0.3 volume fraction led to the 35% increase in Nusselt number compared to applying smooth tubes and water-based fluid. The coefficient of friction with a 0.3% volume fraction of Nanofluid associated with 12 triangular baffles at a 40° angle was, respectively, 5–10% and 1.5 times higher than that of the water flow within a smooth tube without the presence of baffles and Nanofluids. Moreover, results of Perceptron artificial neural network showed that applying a 1-32-4 topology and Levenberg–Marquardt algorithm would derive 0.98828 and 3.6275 values for the mean squared error (MSE) and coefficient of correlation, respectively.

Keywords Carbon/water Nanofluid · Triangular baffle · Artificial neural network (ANN) · Coefficient of friction · Nusselt number

Abbreviations

A	Heat transfer area (m^2)
C_p	Specific heat (kJ kg^{-1} $°C^{-1}$)
d	Diameter (m)
h	Convective heat transfer coefficient (W $m^{-2o}k^{-1}$)
k	Thermal conductivity (W m^{-1} K^{-1})
L	Tube length (m)
m^o	Mass flow rate (kg s^{-1})

✉ Heydar Maddah
heydar.maddah@gmail.com

✉ Mohammad Hossein Ahmadi
mohammadhosein.ahmadi@gmail.com

✉ Mohsen Sharifpur
mohsen.sharifpur@up.ac.za

[1] Department of Chemical Industry, Shahid Rajaei Lahijan Technical College, Technical and Vocational University of Gilan Province, Lahijan, Iran

[2] Department of Chemical Engineering, Imam Hossein University, Tehran, Iran

[3] Department of Process, Energy and Environmental Technology, University of South-Eastern Norway, Notodden, Norway

[4] Department of Chemistry, Science Faculty, Arak Branch, Islamic Azad University, Arak, Iran

[5] Faculty of Mechanical Engineering, Shahrood University of Technology, Shahrood, Iran

[6] Department of Mechanical and Aeronautical Engineering, University of Pretoria, Pretoria 0002, South Africa

[7] Department of Medical Research, China Medical University Hospital, China Medical University, Taichung, Taiwan

[8] School of Mechanical, Industrial and Aeronautical Engineering, University of the Witwatersrand, Private Bag 3, Wits 2050, South Africa

Nu	Nusselt number (Dimensionless)
TPF	Thermal performance factor
MSE	Mean squared error
Q	Heat transfer rate (W)
Re	Reynolds number (Dimensionless)
T	Temperature (^{o}C)
V	Velocity (ms^{-1})
f	Friction factor
pr	Prandtl number (Dimensionless)

Greek symbols

ΔT_{lm}	Logarithmic mean temperature difference (^{o}C)
ΔP_{nf}	Pressure drop
ρ	Density (kg m^{-3})
φ	Nanoparticle volume concentration (Dimensionless)
μ	Viscosity

Subscripts

h	Hot
c	Cold
f	Fluid
i	Inlet
nf	Nanofluid
bf	Base fluid
o	Outlet
p	Particles
w	Wall
b	Bulk

Introduction

There are various methods for improving the heat transfer at industrial scales. Fins, baffles, and spiral conveyors in the flow path of the fluid are used to enhance the heat transfer. A change in the geometry of fins, baffles, and ribs decreases pressure drop and system friction coefficient, improving the system functions. The effect of using baffles and Nanofluids in the heat transfer has been investigated [1–9]. In their study, Kumarasan et al. [10] investigated the impact of baffles deviation and cut percentages on optimizing the heat exchanger performance and found their important role in this regard. Zheng et al. [11] examined four kinds of orifice baffles. Based on the results, the cinquefoil orifice baffles caused the highest increase in the heat transfer coefficient. Zhiya et al. [12] studied a shell and tube heat exchanger with different tube arrangements numerically. In a study, Makool et al. [13] examined the spiral baffle impact on a double-pipe heat exchanger and demonstrated that these baffles increased the heat transfer and pressure drop. Using ANSYS Fluent software, Rao et al. [14] investigated simulation of the shell-side flow in a heat exchange with sector baffles and elliptical tubes. Their findings showed that the heat exchanger with an elliptical tubes performed appropriately. The heat transfer rate increase using copper oxide/water Nanofluid at different concentrations within a spiral conveyor-equipped corrugated pipe was studied by Khanchi et al. [15]. According to their results, for the same heat transfer rate, the friction coefficient increased due to using copper oxide/water Nanofluid. Rousta et al. [16] studied the heat transfer and hydrodynamic performance of the flow using various types of the vortex generator empirically and found that the imperforated rectangular vortex generator had the highest coefficient of friction, but the heat transfer obtained by the biforate trapezoidal vortex generator was slightly higher. The thermal properties and hybrid flow of Nanofluid within the channel associated with rectangular, trapezoidal, and triangular vortex generators were examined by Sheikhzadeh et al. [17]. The findings revealed that the rectangular vortex generators increased the heat transfer ratio and the heat transfer rate increased with an increase in the volume fraction of Nanoparticles enhancement. In a study by Hahn et al. [18], four types of curved vortex generators were investigated. Based on the obtained results, the heat transfer improvement increased because of the fluid flow conductivity enhancement. Abdullahi et al. [19] studied the effects of shape and angles of attack of the vortex generators on the heat transfer. Using the neural network and multi-objective algorithms was considered as the optimal state. In another study by Murthy et al. [20], the heat exchanger performance efficiency obtained due to using aluminum oxide and graphene oxide Nanofluids was assessed. Results revealed the increase in the Nusselt number with 10 baffles. Promvonge et al. [21] studied the baffle efficiency and found an increase in the Nusselt number. Indri Yaningsih et al. [22] investigated the effect of using baffles. Based on the results, the heat transfer and volume fraction increased. In a study by Rashidi et al. [23], thermophysical properties of hybrid Nanofluids were evaluated. Their result showed that the specific heat variation depends on the base fluid, and the increase in temperature increases the thermal conductivity. Ghalandari et al. [24] investigated applications of intelligent methods in different kinds of heat exchangers and concluded that intelligent methods are useful in investigating heat exchanger performance due to their capabilities in exact prediction and fast performance. Kuosa et al. [25] studied a heating system with the ring network technology and plate heat exchangers, and they found almost identical heat capacity flows. Maleki et al. [26] examined thermal conductivity modeling of Nanofluids using ANN and MARS. According to their results, the most accurate model is obtained using ANN with Levenberg–Marquardt. Basit Shafiq et al. [27] investigated thermal performance improvement of shell and helical coil heat exchanger using MWCNTs/water Nanofluid and found that when using this Nanofluid, the highest improvement in Nusselt number was obtained. Mazdak et al. [28] analyzed a heat exchanger with curved segmental

baffle and Cassini oval cross-section tubes in various bundle arrangements numerically. The obtained results revealed the PEC increase with curved baffles.

Samruaisin et al. [29] investigated enhanced heat transfer of a heat exchanger tube installed with V-shaped delta-wing baffle turbulators. They found that eight-wing baffles provided a maximum aerothermal performance factor. Dhumal et al. [30] examined enhancing heat transfer performance in a double-tube heat exchanger with twisted and helical tapes. Based on the results, twist ratios have a critical role in optimizing heat transfer efficiency. Akalin et al. [31] evaluated the preparation, characterization, and antibacterial properties of chitosan/pectin silver Nanoparticle films. Their results showed the increase in the thermal stability due to the presence of pectin. Taner et al. [32] studied a new method for the fresh strawberry package using CMC-based edible coating composite films. Based on their results, the protein and phenolic compounds used in CMC benefited the CMC film-coated strawberry. DALKILIÇ [33], in a study, reviewed flow boiling in mini- and microchannel for enhanced geometries. He found that using these structures is increasing as a result of cooling need in small confined spaces. DALKİLİC [34] examined energy, exergy, and thermoeconomic analyses on vapor-compression system cascaded with libr/water and nh3/water absorption cascade refrigeration cycle. His findings showed that cascade systems' COP values increase due to increasing the generator and evaporator temperatures and they also increase with decreasing the condenser and absorber temperatures.

Previous studies indicated that adding turbulators would have a special effect on the improvement of heat transfer performance. However, investigating the effects of related numbers and angles on the heat transfer performance has not been studied widely. The present study addresses the effects of using triangular baffles with different angles and numbers, as well as carbon/water Nanofluid on the heat transfer, Nusselt number, and coefficient of friction. Adding the triangular baffles, the efficiency of Perceptron ANN, and response surface method to predict the Nusselt number of double-tube heat exchangers are the innovations of the present study.

The laboratory Section

Applied laboratory devices and baffles

In the current experiments, copper triangular baffles at 70° and 40° angles with 1mm thicknesses and numbers of 4, 8, and 12 were located within the copper inner tube of the exchanger (Fig. 1). A 1mm thickness was selected with the purpose of preventing higher frictions.

Triangular baffles with the above-mentioned geometric parameters were located in a round copper tube with the inner and outside diameters of 20 mm and 22 mm, respectively. The outside tube with the water base fluid flow was associated with 25 mm and 27 mm inner and outside diameters, respectively. In order to prevent heat loss and achieve more accurate solutions, the outer wall of the converter is insulated with glass wool and foam, significantly reducing heat loss. According to Fig. 2, a copper double-tube heat exchanger with an 1100 mm length was applied. It included an inner and outside tube that separated the Nanofluid and base fluid. Two numbers of a flow meter (model Flownetix series 100 with $\pm 1\%$ accuracy) and a brass valve were applied to control the carbon/water Nanofluid flow as the hot and cold fluids. Two calibrated RTD-PT 100 temperature sensors with a digital indicator of accuracy 0.1 °C measure the temperature of the entrance and exit of the test area. Also, six flexible thermocouples of K-type, with a temperature range from 15 to 350 °C and accuracy of ± 0.1, are placed on the wall of the flow tube with a distance of 120 mm from each other to measure the temperature distribution of the tube wall. To measure the static (thermodynamic) pressure drop of the Nanofluid flow along the test area, a



Fig. 1 Applied triangular baffles at 70° and 40° angles: **a** 4 baffles; **b** 8 baffles; **c** 12 baffles

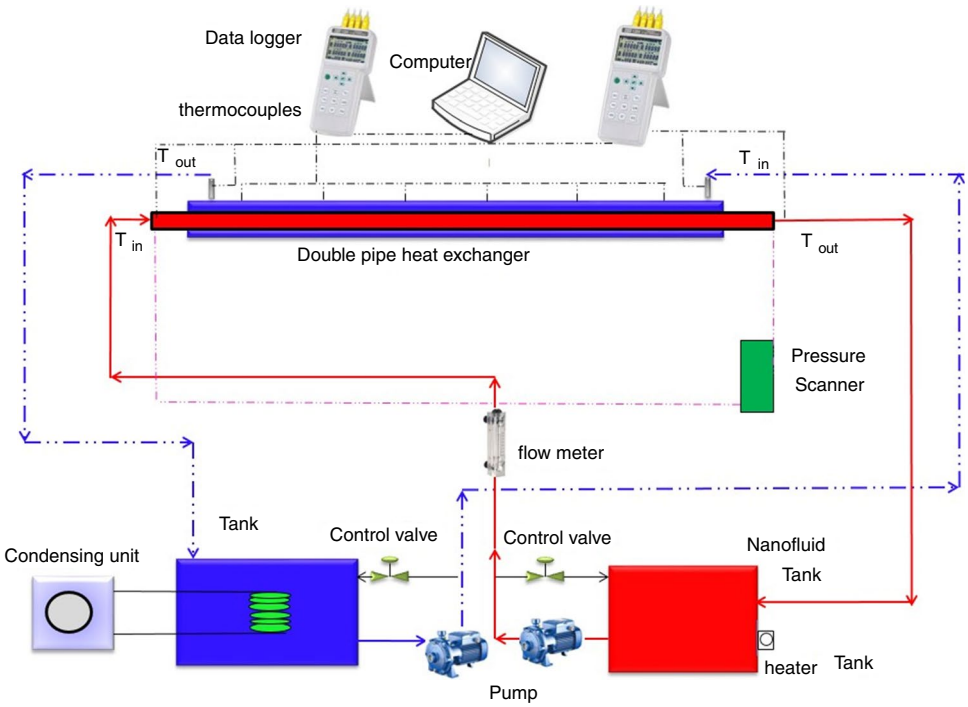


Fig. 2 A double-tube heat exchanger with baffles applied to the inner tube and carbon/water Nanofluid

Table 1 Physical properties of the applied carbon black Nanoparticles

Carbon black Nanoparticles size	25 nm
Powder purity	99.3%
Specific surface area	700 $cm^2\ g^{-1}$
Color	Black
pH	9.62
Moisture content	< 4%
True density (particle density)	≤ 0.35 g cm^{-3}
Electrical conductivity	0.28 S cm^{-1}

3051 cd-type pressure drop transmitter with an accuracy of ± 0.1 was used. This equipment measures the pressure drop between the entrance and exit areas of the test area in each test. A heater equipped with a digital thermostat is used to adjust the temperature of the hot fluid tank (Nanofluid) with the dimensions and specifications of 3 kW, 100 mm × 10 mm (L × D) at the desired temperature. For the rotation of the Nanofluid and the base fluid, two centrifugal, stainless steel impeller model pumps were used. The mentioned triangular baffles were welded on a copper wire at 70° and 40° angles and then located within the inner tube of the exchanger. To measure the fluid flow, an ultrasonic flow meter (manufactured by Flownetix) is installed in trajectory line of fluid. An AC bolt heater (manufactured by Cetal Co.) is installed inside the Nanofluid tank. For water and Nanofluid loops, a refrigerant cooler is installed inside the tank for chilling the warmed water.

Providing the carbon/water Nanofluid

In the current study, the carbon black/deionized water was tested. Nanoparticles were purchased from an American company called Nanomaterials Research US. Table 1 provides the physical properties of applied carbon black Nanoparticles.

To provide the carbon black Nanoparticle, a two-step method was used. The implemented Nanofluid is provided at 0.1–0.3 volume fractions using Eq. 1.

$$\text{Volume concentration, } (\varphi) = \frac{\left(\frac{w}{\rho}\right)_{np}}{\left(\frac{w}{\rho}\right)_{bf} + \left(\frac{w}{\rho}\right)_{np}} \quad (1)$$

where w_{np} is mass of Nanoparticles, w_{bf} is maass of base fluid, ρ_{np} is density of Nanofluid, and ρ_{bf} is density of the base fluid.

To prototype the Nanofluid, 100-cc deionized water was poured into a beaker. Then, the Nanoparticle and surfactant were added based on the calculated mass (< 0.1%). In the following, the mixture was placed in the stirrer at 500 rpm to achieve a steady carbon/water Nanofluid. Next, a 600-W ultrasonic homogenizer was applied for 3–6 h to reach a steady particle suspension. The evaluation of Nanofluid stability was carried out through related electrical conductivity at various pH values. The volume fractions of Nanoparticles applied to the current study were determined to be 0.2, 0.3, and 0.1 volume percent in a 25 nm diameter.

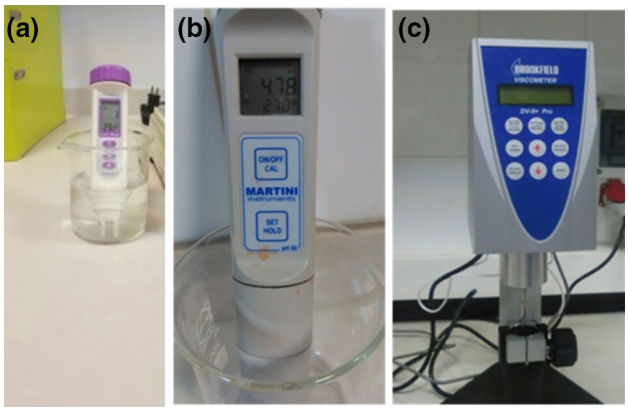


Fig. 3 **a** AZ electrical conductivity meter; **b** pH meter; and **c** Brookfield viscometer

To conduct the process of pH measurement, a Milwaukee pH56 waterproof with replaceable probe was applied in a range of 2 to 10. Also, the device temperature range was 0.5–60 °C (Fig. 3). The prototype remained stable for a few weeks without any sedimentation. The Nanofluid electrical conductivity was tested using AZ8351 device made by Taiwanese Az Company (Fig. 3a). The range of testing conductivity was determined to be 0–20000 µS with a 1% resolution. The range of temperature measurement of the device was between 0 and 50 °C with a 0.1 °C temperature resolution. The achieved values of electrical conductivity for water base fluid and Nanofluid with volume fractions of 0.1, 0.2, and 0.3 volume percent at pH values of 6.80, 7.1, 7.3, and 7.4 were, respectively, determined to be 530, 684, 794, 898, and 1056 µS/cm.

Measurement of the coefficient of thermal conductivity, viscosity, and electrical conductivity

To calculate the Nanofluid coefficient of thermal conductivity and viscosity, the transient hot-wire technique was applied using Pro-KD2, Probe KS1, and Brookfield viscometer (Fig. 3c). The spindle speed was in the range of 0–100 rpm.

Uncertainty analysis

To measure the heat transfer parameters uncertainty, the following equation could be applied.

Table 2 The percent error for laboratory parameters

Parameter	Uncertainty error
Nanofluid heat transfer	1.9%
Nusselt number	1.76%
Coefficient of friction	1.97%

$$R = \left[\sum_{j=1}^{M}\left(\frac{\delta R}{\delta X_j}\delta X_j\right)^2\right]^{\frac{1}{2}} \tag{2}$$

where δR, δX_j, M, and j are, respectively, the specific mutual parameters, as well as the quantity of R-dependent and X_j -independent variables. The values of uncertainty error and resulted percent errors are provided in Tables 2 and 3.

Governing equations

The Nanofluid viscosity ($\boldsymbol{\mu_{nf}}$), specific heat capacity ($\mathbf{C_{P_{nf}}}$), and density ($\boldsymbol{\rho_{nf}}$) can be computed using the following equations [14].

$$\mu_{nf} = \mu_{bf} + (1 + 2.5\varphi) \tag{3}$$

$$C_{P_{nf}} = \varphi C_{PP} + (1 + \varphi)C_{Pbf} \tag{4}$$

$$\rho_{nf} = \varphi\rho_p + (1 - \varphi)_{\rho_{bf}} \tag{5}$$

The indices bf, nf, and p indicate the base fluid, Nanofluid, and Nanoparticle, respectively.

The Reynolds number, Nanofluid heat transfer, base fluid, average heat transfer, as well as log mean temperature difference, are, respectively, shown in Eqs.6–10.

$$\mathrm{Re} = \frac{\rho V d}{\mu} \tag{6}$$

$$Q_h = m_h^{\circ} C_{ph}\left(T_{hi} - T_{ho}\right) \tag{7}$$

$$Q_c = m_c^{\circ} C_{pc}\left(T_{co} - T_{ci}\right) \tag{8}$$

$$Q_{ave} = \frac{Q_h + Q_c}{2} \tag{9}$$

$$\Delta T_{LM} = \frac{\left(T_{hi} - T_{co}\right) - \left(T_{ho} - T_{ci}\right)}{\mathrm{In}\left[\frac{T_{hi} - T_{co}}{T_{ho} - T_{ci}}\right]} \tag{10}$$

Table 3 Percent errors considered for laboratory devices

Device	Device measurement range	Measurement parameter	Minimum calibrating	Experimental minimum and maximum measurements	Instability
Flowmeter	0–28 L min^{-1}	Volumetric flow type	0.01 L min^{-1}	2–10 L min^{-1}	0.18%
Temperature thermocouple (data logger)	50–200 °C	Flow temperature	0.1 °C	30–55 °C	0.23%
Temperature thermocouple (data logger)	73–260 °C	Wall temperature	0.1 °C	30–65 °C	0.61%
Pressure transmitter	0–20000 Pa	Pressure	10 Pa	100–1700 Pa	0.66%

In these equations,$\dot{m}_h$, $\dot{m}_c$,C_{ph}, and C_{pc} are the flow rate of hot and cold fluids and the heat capacity of hot and cold fluids, respectively.

The Nanofluid convection heat transfer coefficient, Nusselt number, and coefficient of friction could also be calculated as the following, respectively.

$$h = \frac{Q_{surf}}{A_{surf} \times \left(T_s - T_b\right)} \tag{11}$$

$$\mathrm{Nu} = \frac{\mathrm{hd}}{k} \tag{12}$$

$$f_{exp} = \frac{\Delta p_{exp}}{\left(\frac{L}{d}\right)\left(\frac{\rho v^2}{2}\right)} \tag{13}$$

According to the above equations, the heat transfer surface (Q_{surf}), tube wall temperature, and bulk temperature, which is the average of Nanofluid inlet and outlet, were, respectively, shown by A_{surf}, T_w, and T_b.

The coefficient of friction factor, pressure difference, density, and length were also identified by f_{exp}, Δp_{exp}, ρ, and L.

The thermal performance factor, which is a performance evaluation criteria applied to compare the conditions of tube-embedded triangular baffles and baffles removal from smooth tubes, would be achieved as the following.

$$\mathrm{TPF} = \frac{\left[\frac{\mathrm{Nu}}{\mathrm{Nu}_{\text{plain tube}}}\right]^{1/3}}{\left[\frac{f}{f_{\text{plain tube}}}\right]^{1/3}} \tag{14}$$

Optimization using the response surface method

In the current study, the data analysis and optimization of heat transfer process were carried out using the response surface method. Trials were conducted based on the central-composite design using Minitab 18 software. Trial points of the central-composite design included the main, axial, and central points. According to the mentioned design, the number of experiments is calculated using Eq. 1.

$$N = 2^u + 2u + C_0 \tag{15}$$

where N, u, 2^u, $2u$, and C_0, respectively, show the numbers of trials, parameters, main points-related trials, axial points-related trials, and central point iteration-related trials. The quantity of iteration points depends upon the number of variables determined by the software, which could be applied to the error calculation. In the current study, the central-composite design was defined with 30 trials considering the selection levels. The levels of the encoded independent variables of a double-tube heat exchanger are provided in Table 4.

The basis of response surface method is the two-level factorial designs. The linearity assumption considered for factorial effects is the main reason of applying the two-level factorial designs. To conduct a behavioral modeling of the mentioned systems, Eq. 16 is implemented.

$$y = \beta_0 + \sum_{j=1}^{k} \beta_j x_j + \sum \sum_{i<j=2}^{k} \beta_{ij} x_i x_j \tag{16}$$

where the response variable, model constant, number of variables, coefficients of variables, independent variable, and coefficient of variables cross-impacts are, respectively, shown by β_0, k, β_j, x_j, and β_{ij}. This is a first-degree

Table 4 Levels of encoded independent variables of a double-tube heat exchanger

Variable	Encoded levels of the variable		
	1	0	−1
Reynolds number	4000	8000	14,000
Nanofluid volume fraction	0	0.15	0.3
Baffles number	4	8	12
Baffles angles	40		70

polynomial model, which is only suitable to show some curvatures of the response function. Equation 17, which is called the second-order response surface model, is applied to cases wherein the model was not able to model the response function curvatures.

$$y = \beta_0 + \sum_{j=1}^{k} \beta_j x_j + \sum \sum_{i<j=2}^{k} \beta_{ij} x_i x_j + \sum_{j=1}^{k} \beta_{jj} x_j^2 \quad (17)$$

According to the above equation,β_{jj} showed the coefficient of the second-order parameter. Due to the fact that the quantity of β s is higher than that of treatments, the two-level multi-factorial design with central and real points could not be applied to estimate the variable coefficients (β s) of a second-order model. Therefore, β s calculation and more appropriate application of the second-order model would be achieved through adding the axial points.

ANN-based optimization process

In the current study, the process of ANN-based optimization was first carried out through normalizing the experimental data. Then, SUM variable was defined as the optimization index considering the importance of response variables and assigning the mass factors. To create artificial networks for the double-tube exchanger, various parameters were applied as the input of network instruction and evaluation. These parameters included the Reynolds number, Nanofluid volume fraction, as well as baffles quantity and angles. Moreover, Nusselt number was considered as the target or output.

Normalization

The experimental data are normalized to increase the network speed and accuracy with the purpose of the value equalization of the input data using Eq. 18. The process of normalization prevented the over-mass loss [7].

$$X_n = \frac{X_i - X_{min}}{X_{max} - X_{min}} \quad (18)$$

where the parameter normalized quantity, real value of each parameter, as well as maximized and minimized values of the considered parameter, were, respectively, shown by X_n, X_i, X_{max}, and X_{min}.

ANN implementation

A number of 30 empirical tests were conducted for double-tube heat exchangers. After the data normalization and achieving the SUM factor for each test, 75% of data were randomly selected for the network instruction and the remaining 25% were applied to the process of instructed networks evaluation. Then, the normalized and SUM factor data were the ANN toolbox input using R2009a MATLAB software in the form of four transpose matrixes. Therefore, the feed-forward back propagation (FFBP) and cascade-forward back propagation (CFBP), which are considered as the most important ANNs applied to the engineering issues and scientific calculations, were selected [7]. Then, the instruction input and output data were selected. Considering the instruction functions, Levenberg–Marquardt algorithms were applied. Then, a three-layer Perceptron network was tested to determine the optimal structure. The schematic structure of the three-layer Perceptron network is shown by Fig. 4. The first layer was data entry without any processing, the second hidden layer conducted the processing, and the last layer provided the output and processed data for the user or system. There are 1–40 neurons determined for the middle layer. To create a network, PURELIN, TANSIG, and LOGSIG functions were selected. The input and output parameters used in the analysis are represented in the table below (Table 5).

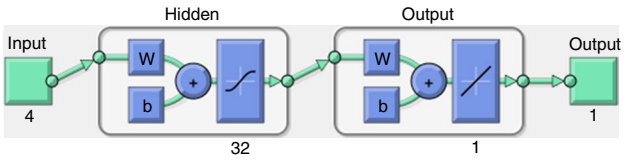


Fig. 4 The schematic structure of a three-layer Perceptron neural network to predict the Nusselt number

Table 5 Input and output parameters used in the analysis

Input	Output
Reynolds number	Nusselt number
Nanofluid volume fraction	
Baffles number	
Baffles angles	

To analyze and find a network with an appropriate topology using the instruction algorithm, several quantitative indexes were applied. The following criteria were applied to determine the quality of network performance in the current study: The mean squared error (MSE) was implemented with the purpose of minimizing the mentioned error. Decreased values of the mentioned error led to the reduction of difference between the real and predicted values, which are achieved using Eq. 19.

$$MSE = \frac{\sum_{i=1}^{n} (Nu_i \hat{N}u_i)^2}{n} \quad (19)$$

$$R = 1 - \frac{\sum_{i=1}^{n}(Nu_i - \widehat{Nu}_i)^2}{\sum_{i=1}^{n}(Nu_i - \overline{Nu})^2} \quad (20)$$

where Nu_i, $\widehat{Nu}_i$, $\overline{Nu}$, and n are experimental data, predict data, the average value of experimental data, and the number of data points, respectively.

Discussion and conclusion

Validation of the coefficient of thermal conductivity, viscosity, and heat transfer parameters

The temperature and volume fraction are considered as the parameters with significant effects on coefficients of thermal conductivity of Nanofluids. Therefore, the coefficients of thermal conductivity could be recognized as a function of temperature and volume fraction that could change as a result of transformations in the mentioned parameters. The volume fraction is the only parameter represented in most of the classical and empirical models to estimate the coefficient of thermal conductivity of Nanofluids. The volume fraction- and temperature-based changes in the coefficient of thermal conductivity of carbon/water Nanofluid are shown in Fig. 5. These changes were associated with a similar process with different slopes for each temperature and volume fraction. According to Fig. 5, increased temperature and volume fraction would enhance the coefficient of thermal conductivity of Nanofluid. The main causes of increased coefficient of thermal conductivity could be attributed to various factors. Nanofluid molecules were associated with specific kinetic energies at determined temperatures. As the temperature increased, the kinetic energy, Brownian motions of Nanoparticles and, consequently, the coefficient of thermal conductivity of Nanofluids would enhance. On the other hand, the increased number of Nanoparticles suspended within the fluid enhanced the coefficient of thermal conductivity. This could be attributed to various factors, such as increased surface to volume ratio, clustering, and collision of Nanoparticles. Due to the mentioned reasons, a significant enhancement could be observed in the coefficient of thermal conductivity as a result of the simultaneously increased temperature and volume fraction.

According to Fig. 5, the coefficient of thermal conductivity linearly increased. The mentioned enhancement was associated with an increased slope at > 0.1 volume fractions. In other words, the temperature changes could highly influence the Nanofluids coefficient of thermal conductivity at higher volume fractions. Considering the minimal volume fraction (0.1), a double increase in temperature, which was 35 °C to 55 °C, led the Nanofluids coefficient of thermal conductivity to increase from 0.62 to 0.71 $W/m^{-1}\,K^{-1}$. Meanwhile, the coefficient of thermal conductivity increased from 0.62 to 0.71 $W/m^{-1}\,K^{-1}$ at the highest volume fraction (0.3) in the similar temperature range of 35–55 °C. According to Fig. 6, changes in the viscosity of carbon/water Nanofluid with a shear stress at different volume fractions of the Nanofluid were between 0.1 and 0.3%. The viscosity tests were carried out at 20 °C. It is concluded that the shear viscosity increased as a result of the volume fraction enhancement of carbon/water Nanofluid. This could be due to the fact that the increased number of carbon black Nanoparticles would increase the influence of Nanoparticles on the base fluid-derived atoms. Consequently, the Van der Waal force between particles enhanced, which prevented the heat transfer between layers and increased the dynamic viscosity. As a result of increased shear velocity, the mass structures of Nanoparticles were broken and led to the viscosity enhancement. The Nanoparticles interactions and resisting force enhancement were achieved due to the increased volume fraction of Nanofluid. Therefore, the viscosity and thermal resistance could be increased as a result of the volume fraction enhancement.

Results of initial tests applied to validate the laboratory system structured for the water base fluid in a smooth tube

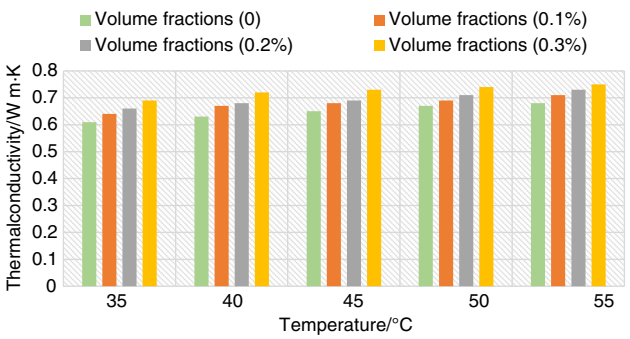


Fig. 5 The temperature-based changes in the coefficient of thermal conductivity for different volume fractions of carbon/water Nanofluid

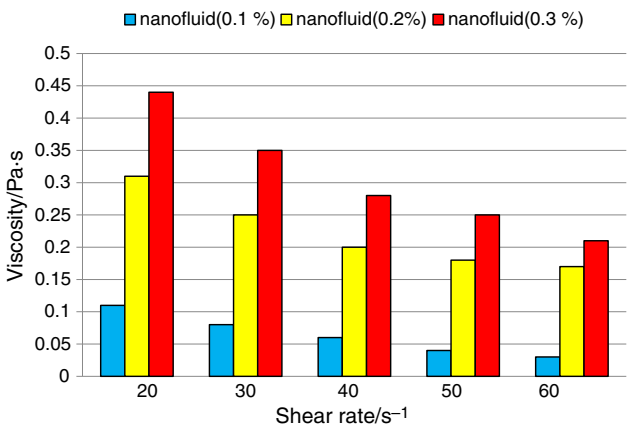


Fig. 6 Viscosity changes with shear stress for different volume fractions of carbon/water Nanofluid

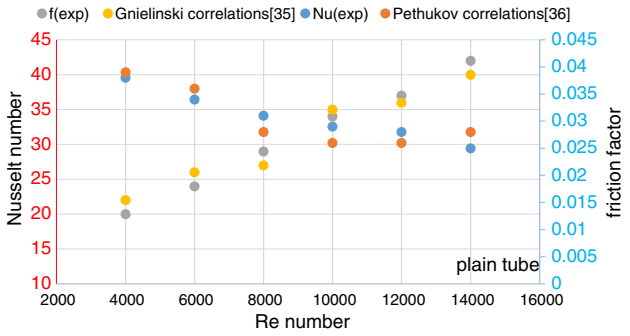


Fig. 7 A comparison between Nusselt number and coefficient of friction factor for the water base fluid in a smooth tube

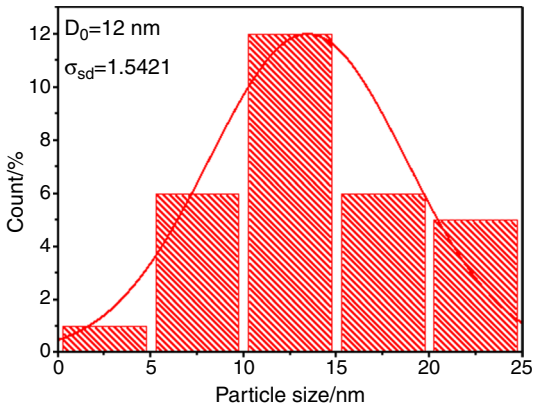


Fig. 8 Particle size distribution fitted with a log normal distribution function for carbon black Nanoparticles. (Color figure online)

are shown by Fig. 7. The achieved findings were compared with those of Gnielinski and Pethukov [35, 36]. As it could be observed, the experimental data of Nusselt number and coefficient of friction were in a good accordance with the theoretical models. Moreover, the deviations between real and theoretical values related to Nusselt number and coefficient of friction were determined to be almost 3.8 and 3.6%.

$$\mathrm{Nu} = \frac{\left(\frac{f}{8}\right)(\mathrm{Re} - 1000)\mathrm{pr}}{1 + 12.7\left(\frac{f}{8}\right)^{\frac{1}{2}}\left(\mathrm{pr}^{\frac{2}{3}} - 1\right)} \tag{21}$$

$$f = (0.78\ln\mathrm{Re} - 1.64)^{-2} \quad 3000 < \mathrm{Re} < 5 \times 10^{6} \tag{22}$$

The Nanoparticles size and standard deviation

The Nanoparticles size and standard deviation for carbon black are almost 12 nm and 1.5421 nm, respectively (Fig. 8).

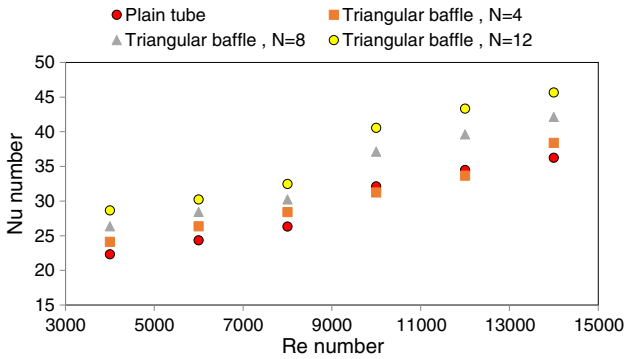


Fig. 9 Nusselt number values achieved for the triangular smooth tubes with 4, 8, and 12 triangular baffles embedded at a 70° angle without the presence of Nanofluid

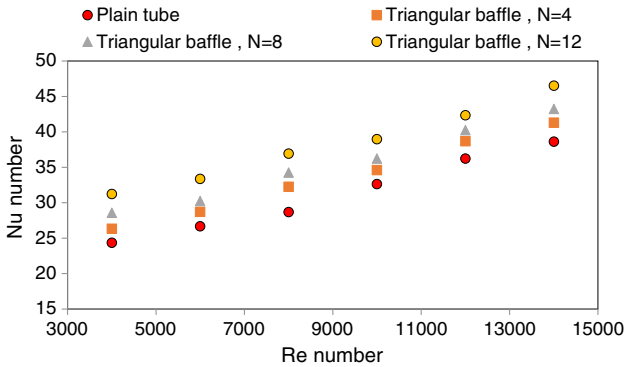


Fig. 10 Nusselt number values achieved for the triangular smooth tubes with 4, 8, and 12 triangular baffles embedded at a 40° angle without the presence of Nanofluid

The analysis of Nusselt number achieved using 4, 8, and 12 triangular baffles at 70° and 40° angles

According to Figs. 9, 10, the effects of applying 4, 8, and 12 triangular baffles at 70° and 40° angles within the inner tube were found. As it could be observed, Nusselt number increased as a result of the enhanced baffles quantity, decreased baffle angles, and increased Reynolds number. As an example, four 70° triangular baffles that could derive 22.36, 24.15, 26.39, and 28.69 Nusselt numbers were achieved at 4000 Reynolds number. Meanwhile, these values were, respectively, determined to be 24.36, 26.35, 28.6, and 31.25 under similar conditions at a 40° angle. The implementation of triangular baffles within tubes would considerably increase the heat transfer, specifically at higher flow rates. Moreover, it could cause a strong turbulence within the tube and, consequently, a fast turbulence between the core and wall flow of the inner tube. This would increase the base water fluid Nusselt number. In other words, the increase in baffles from 4 to 8 and 12 could form higher longitudinal and cross-flows, as well as a natural vortex along the tube. This

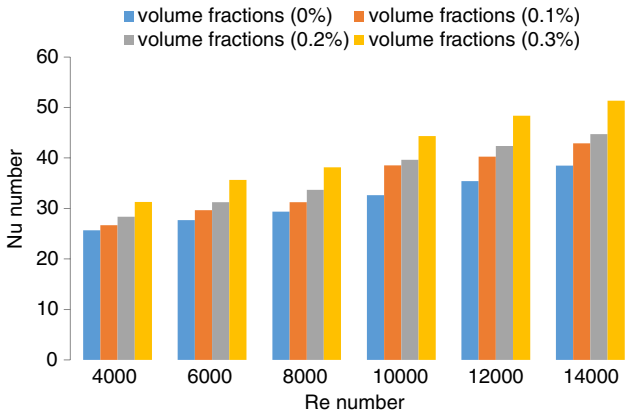


Fig. 11 Nusselt number values achieved for the triangular smooth tubes with 4 triangular baffles embedded at a 70° angle in the presence of carbon/water Nanofluid

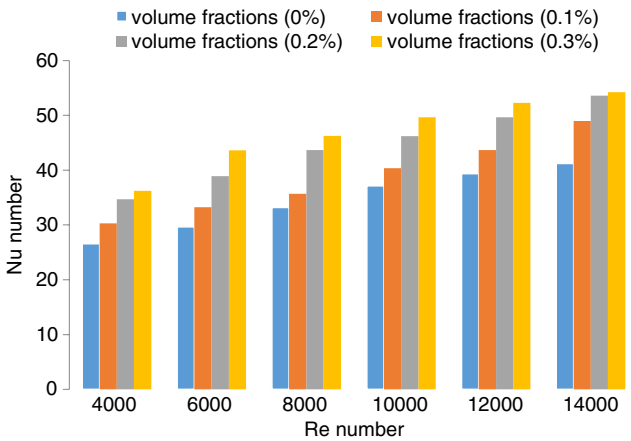


Fig. 12 Nusselt number values achieved for the triangular smooth tubes with 8 triangular baffles embedded at a 70° angle in the presence of carbon/water Nanofluid

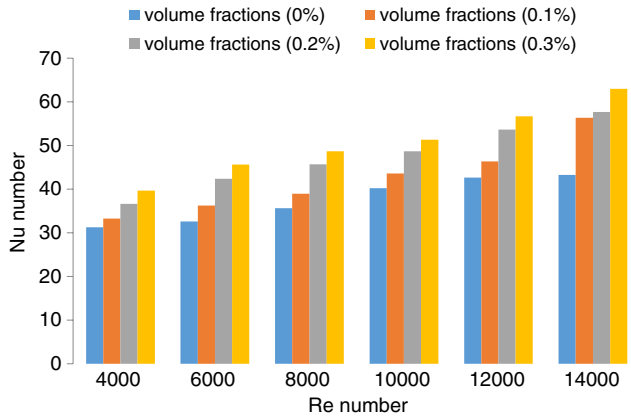


Fig. 13 Nusselt number values achieved for the triangular smooth tubes with 12 triangular baffles embedded at a 70° angle in the presence of carbon/water Nanofluid

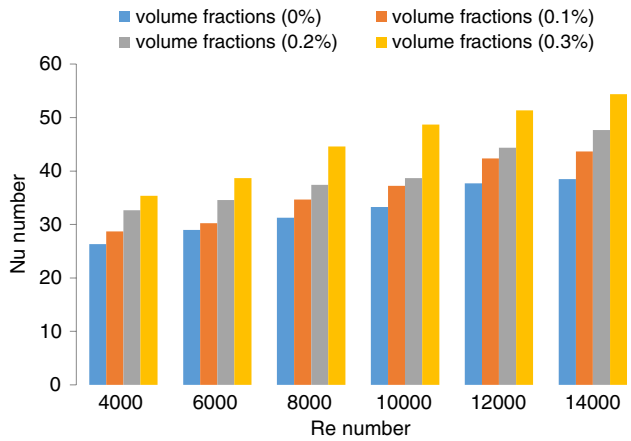


Fig. 14 Nusselt number values achieved for the triangular smooth tubes with 4 triangular baffles embedded at a 40° angle in the presence of carbon/water Nanofluid

could facilitate the more appropriate and faster turbulence of the fluid between the core and farther areas and, consequently, the gradient of higher temperatures near the tube wall. A collision would rapidly occur between the flow and the next baffle while applying 12 triangular baffles due to their insignificant spaces. Consequently, the velocity would increase; however, the decreased number of triangular baffles within the inner tube of Nanofluid was associated with a larger space and time to reach the next baffle. Therefore, the related velocity would decrease.

Changes in Nusselt number with different quantities of triangular baffles embedded at 70° and 40° angles in the presence of carbon/water Nanofluid at 0.1–0.3 volume fractions are shown in Figs. 11– 16. Compared to the water base fluid, a higher Nusselt number was observed for all volume fractions of carbon/water Nanofluid. The mentioned

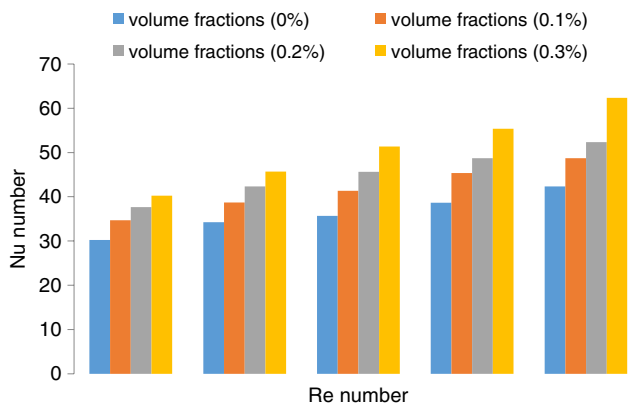


Fig. 15 Nusselt number values achieved for the triangular smooth tubes with 8 triangular baffles embedded at a 40° angle in the presence of carbon/water Nanofluid

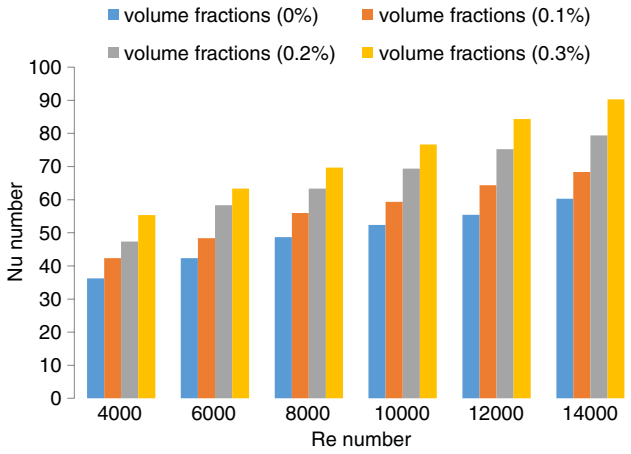


Fig. 16 Nusselt number values achieved for the triangular smooth tubes with 12 triangular baffles embedded at a 40° angle in the presence of carbon/water Nanofluid

increased heat transfer of Nanofluid could be due to several issues, including the enhancement of thermal conductivity, mixing the effects of Nanoparticles near the wall, Brownian motion of Nanoparticles, as well as decreased thickness of the boundary layer. This showed that the application of Nanofluid was more efficient to increase the heat transfer ratio within a triangular baffles-equipped tube. According to Figs. 11– 16, a higher Nusselt number was achieved at 0.3 volume fraction. A 90.32 Nusselt number was achieved under the same conditions, 14,000 Reynolds number, and implementation of 12 baffles at 40°. This indicated the fact that the effects of carbon black Nanoparticles within the base fluid on the heat transfer enhancement would be increased as a result of applying more baffles and decreasing the angles from 70° to 40°. Moreover, it was found that the maximum enhancement of Nusselt number was determined to be 36%. It is noteworthy that according to thermophysical properties measurements, the Nanofluid was associated with higher dynamic viscosity and density compared to water base Nanofluid. Therefore, the density indicated an increase in Reynolds number, while the dynamic viscosity possessed an inverse nature. The high volume fractions of the Nanofluid and increased quantity of triangular baffles indicated a higher heat transfer velocity within a triangular baffles-equipped tube compared to smooth tubes with similar pumping powers. The data achieved from Figs. 11– 16 showed that under similar engineering and operating conditions, a triangular baffles-equipped double-tube heat exchanger was associated with the maximum Nusselt number compared with the smooth tubes. It could be concluded that two considerable factors influenced the fluid flow and heat transfer distribution as a result of the increased surface of triangular baffles-equipped tubes. These factors included the increased heat exchange area between the tube and Nanofluid, as well as increased flow turbulence within the tubes width due to the baffles embedment on the tubes surface.

Figure 17 shows the simultaneous effect of two parameters on Nusselt number. According to the figure, Nusselt number would increase in the vortex-included areas due to the presence of triangular baffles. Considering the space between the mentioned area and the next baffle, the vortex effect and turbulence would decrease and lead to an optimal development. The Nusselt number distribution and related maximum amount changed as a result of increasing the quantity of baffles from 4 to 12. Nusselt number was significantly increased due to the baffles enhancement, as the maximum amount of Nusselt number was determined to be 25 under the conditions of lack of baffles, applying a smooth tube, and 14,000 Reynolds number. However, it increased as a result of applying 4, 8, and 12 baffles at the same Reynolds number. This could be due to the fact that the fluid deviation resulted from triangular baffles at higher Reynolds numbers generated stronger and more massive vortexes. Under the conditions of higher input flow momentum, the baffles acted as obstacles against the flow more efficiently. At higher momentum values, they were associated with stringer and more massive vortex. The quantity and size of generated vortexes around baffles were also changed as a result of increasing the baffles from 4 to 8 and 12. Due to the increase in triangular baffles, more areas around baffles would be associated with less cross-section and higher velocities. This could increase the convection heat transfer compared to the conducting heat transfer and, consequently, enhance the Nusselt number. Despite increased cross-section and convection heat transfer in the area under the baffles, the eddy current and turbulence would be more efficient to raise the coefficient of heat transfer and Nusselt number as a result of extending the baffles quantity.

The Nusselt number values achieved as result of the binary factors are shown in Fig. 18. According to all of the figures, the Nusselt number incremental results were associated with the extended baffles quantity, Reynolds number, Nanofluid volume fraction, as well as baffles angles. It could be said that decreased baffles angles would raise vortexes quantities; moreover, the Nanofluid volume fraction would influence the mentioned parameter and increase the Nusselt number considerably. On the other hand, the time span required for temperature changes would decrease at the Nanoscale. The decreased time span required for complete temperature changes in Nanoparticles could provide enough time for the particles complete temperature changes while contacting the cooling tubes. Also, the enhancement of Nanoparticles volume fraction from 0.1 to 0.2 and 0.3 could increase the number of contacts with cooling tubes and, consequently, Nusselt number. According to Fig. 18, the order of calculated curves disarranged, and related slopes changed due to the extended volume fraction of carbon/water Nanofluid.

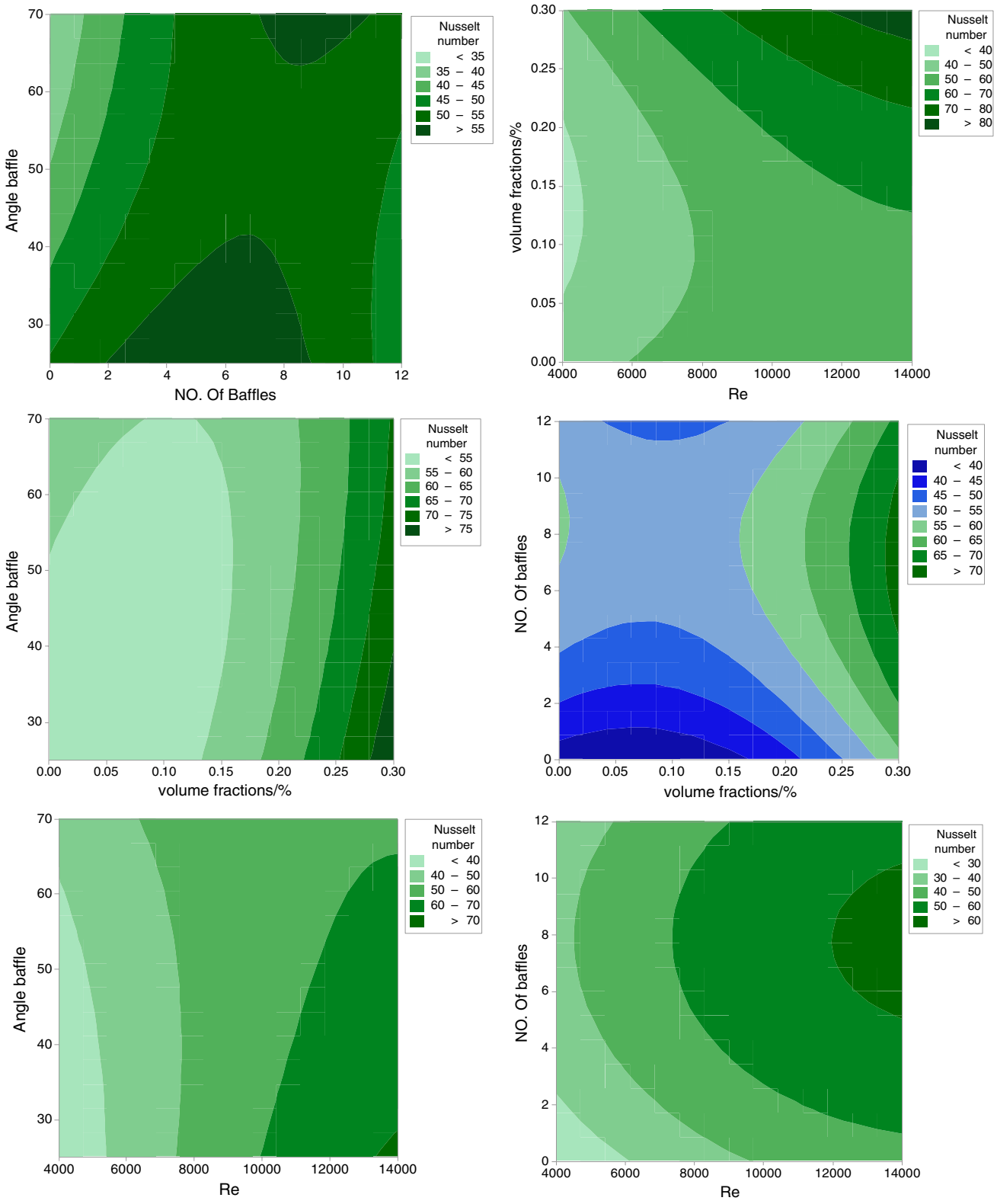


Fig. 17 The simultaneous effect of binary parameters on the achieved Nusselt number

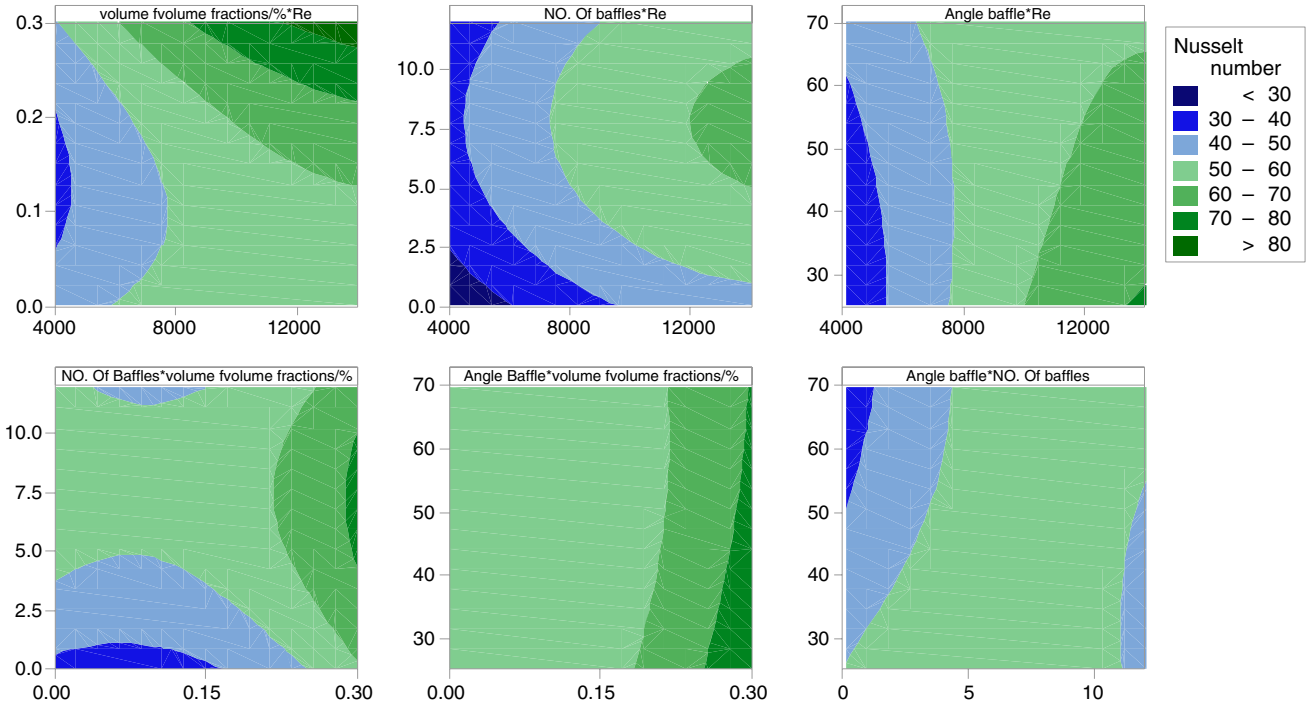


Fig. 18 The effect of binary parameters on the achieved Nusselt number

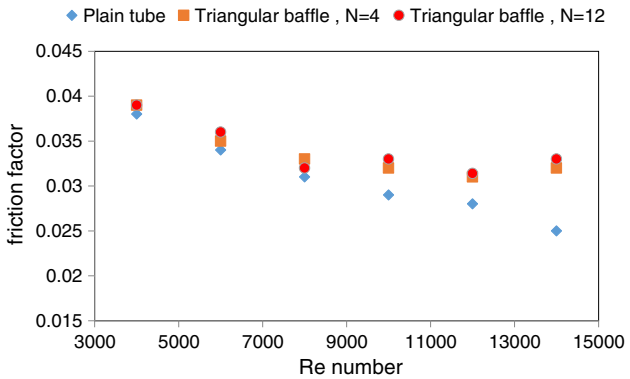


Fig. 19 Values calculated for the coefficient of friction of the smooth tubes and tubes with 4 and 12 triangular baffles at a 70° angle

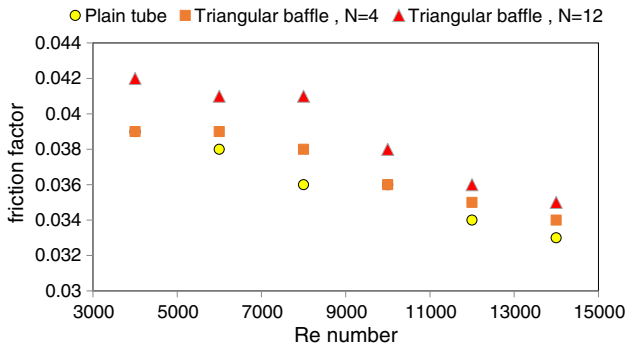


Fig. 20 Values calculated for the coefficient of friction of the smooth tubes and tubes with 4 and 12 triangular baffles at a 40° angle

The changes in coefficient of friction related to the smooth tubes as well as tubes with 4 and 12 triangle baffles at 70° and 40° angles are shown in Figs. 19, 20. As it could be observed, the enhancement of Reynolds number decreased the coefficient of friction. There was not a significant difference between the coefficient of friction found for the smooth tubes and those with triangular baffles. However, the pressure drop factor could be considered. According to Figs. 19, 20, the decreased number of triangular baffles diminished the coefficient of friction. This could be due to the fact that in case of applying more baffles, the baffle spacing would decrease and lead to the fluid flow acceleration and, consequently, increase its contacts with triangular baffles. Therefore, the turbulence would increase and cause the flow path pressure drop within the inner tube. In fact, the baffle spacing causes pressure drop. However, the decrease in baffles quantity could extend the flows motion range, decrease its velocity, and reduce the pressure resulted from contacts with triangular baffles. According to the figure, the coefficient of friction of the smooth tubes using the water base fluid and those of tubes with 4 and 12 triangular baffles at 70° and 40° angles with 4000 and 14,000 Reynolds numbers was, respectively, determined to be 0.038, 0.026, 0.039, 0.033, 0,039, and 0.034.

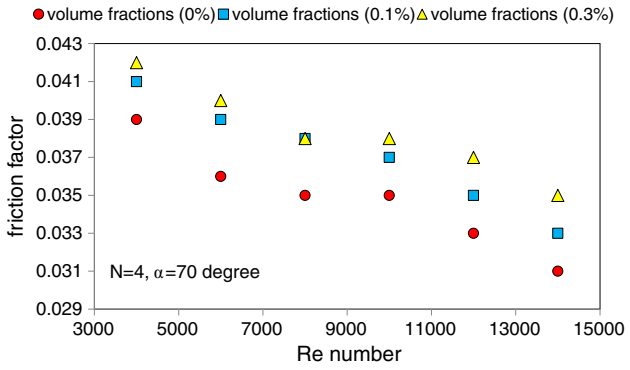


Fig. 21 The coefficient of friction values determined for the tubes with 4 triangular baffles at a 70° angle using the Nanofluid

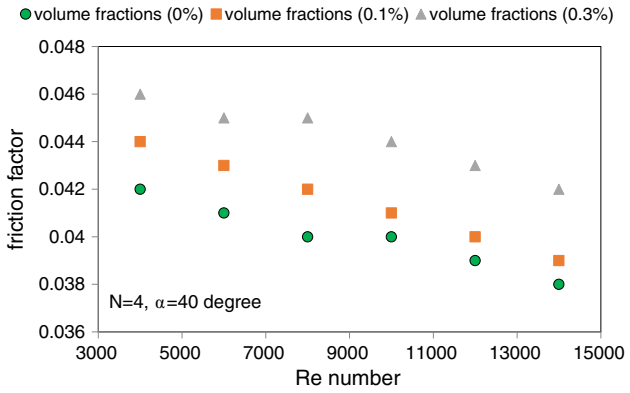


Fig. 22 The coefficient of friction values determined for the tubes with 4 triangular baffles at a 40° angle using the Nanofluid

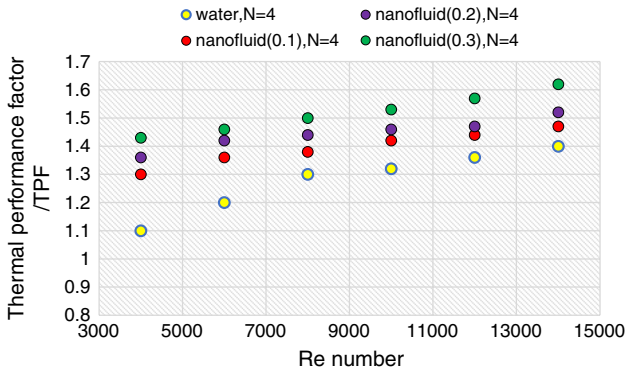


Fig. 23 Values achieved for the heat efficiency factor of the tube with 4 triangular baffles at a 70° angle in the presence of the Nanofluid

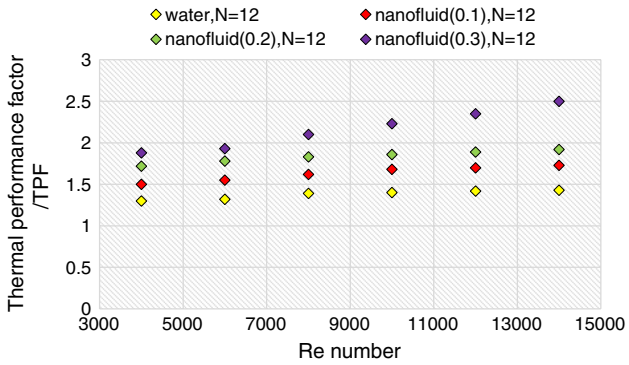


Fig. 24 Values achieved for the heat efficiency factor of the tube with 12 triangular baffles at a 40° angle in the presence of the Nanofluid

The values achieved for the coefficient of friction related to the tube with 4 and 12 triangular baffles at 70° and 40° angles using the Nanofluid at different volume fractions of 0.1–0.3 are shown in Figs. 21, 22. The presence of Nanofluid could be attributed to the fact that the pressure drop of Nanofluid flow at higher volume fractions exceeded the base fluid. Moreover, the flow velocity of Nanofluid was higher than that of water base fluid at the tube inlet due to the high viscosity of carbon/water Nanofluid at a constant Reynolds number. Therefore, the water base fluid flows pressure drop was lower than that of the Nanofluid flow. The increased concentration of Nanoparticles led to the pressure drop enhancement of the Nanofluid and, consequently, its coefficient of friction.

The heat efficiency factor related to the tube with 4 and 12 triangular baffles at different angles is shown in Figs. 23, 24. It could be observed that there was a significant difference between TPE values of the water base fluid and Nanofluid, which were achieved through increasing the baffles quantity and volume fraction from 0.1 to 0.3. It is noteworthy that effect of Reynolds number on 12 baffles was considerably higher than that of 4 baffles. As an example, the extension of Reynolds number from 4000 to 14,000 led to the 5.1 to 15.6% enhancement of TPE values while applying 4 and 12 baffles, respectively. Considering the inner tube with 4 triangular baffles, it was found that the high velocity could be observed behind the primary zone, or the tip, of the baffle contact area. The velocity decreased along the tube; however, it was higher than that of the simple tubes. Extending the triangular baffles to 12 and retaining the heat transfer surface led to the velocity acceleration behind the baffles, coverage of more width of the exchanger tubes surface and, consequently, turbulence enhancement. The mentioned quantity of baffles increased the level of velocity across the tube and along the inner tube. Consequently, the turbulent flow increased in the total area behind the baffles, which could extend the heat transfer and Nusselt number. However, the minimum Nusselt number was found for the simple tube, which could be due to the uniform movement of Nanofluid flow within the tube and lack of an adequate heat transfer between the tube wall and flow.

The residuals chart of Nusselt number is shown in Fig. 25. The deviation from basic assumptions and model adequacy

would be possible through investigating the residuals. The closeness of residuals chart and the standard normal distribution chart, as well as lack of outliers, indicated the fact that the assumption of normality was held (Fig. 25a). Also, the failure of residuals to follow a pattern implied that the grid independence assumption was held (Fig. 25b). Residuals around the base line were arranged randomly without following any specific pattern. Moreover, they were associated with positive and negative values (Fig. 25c), which indicated the independency of data and residuals. As it could be observed, the data distribution was close to the transversal line. This indicated the fact that errors were associated with a normal distribution and the fitted model possessed an appropriate quality (Fig. 25d). As it can be observed in Fig. 26, the single, binary, and triad parameters were shown considering the 95% efficiency. The maximum influence on Nusselt number was resulted from single parameters, such as Reynolds number and volume fraction of Nanoparticles, as well as binary parameters, such as Reynolds number and volume fraction of Nanofluid, and the square of baffles quantity. It is found from Fig. 27 that the importance of parameters in the process of calculating Nusselt number would increase due to the extended distance between parameters and the red line in the chart. However, this could raise their influences on the heat transfer process. Compared to the Nanofluid volume fraction, Fig. 27 shows that Nusselt number was highly influenced by Reynolds number due to its high distance from the mentioned red line.

The resulted quadratic equation represented the relationship between the general changes in Nusselt number and independent variables. As it could be observed, the effects of single, binary, and triad parameters were clear, and the coefficients of equation were determined using Minitab 18.

$$\begin{aligned}\text{Nusselt number} &= 3.3 + 0.00730\text{Re} - 61\text{volumefractions}(\%) \\ &+ 2.12\text{NO.OfBaffles} - 0.04\text{AngleBaffle} \\ &- 0.000000\text{Re} * \text{Re} + 414\text{volumefractions}(\%) \\ &* \text{volumefractions}(\%) - 0.258\text{NO.OfBaffles} \\ &* \text{NO.OfBaffles} + 0.0033\text{AngleBaffle} * \text{AngleBaffle} \\ &+ 0.00800\text{Re} * \text{volumefractions}(\%) - 0.000006\text{Re} \\ &* \text{NO.OfBaffles} - 0.000050\text{Re} * \text{AngleBaffle} \\ &- 2.08\text{volumefractions}(\%) * \text{NO.OfBaffles} \\ &- 1.17\text{volumefractions}(\%) * \text{AngleBaffle} \\ &+ 0.0417\text{NO.OfBaffles} * \text{AngleBaffle}\end{aligned}$$

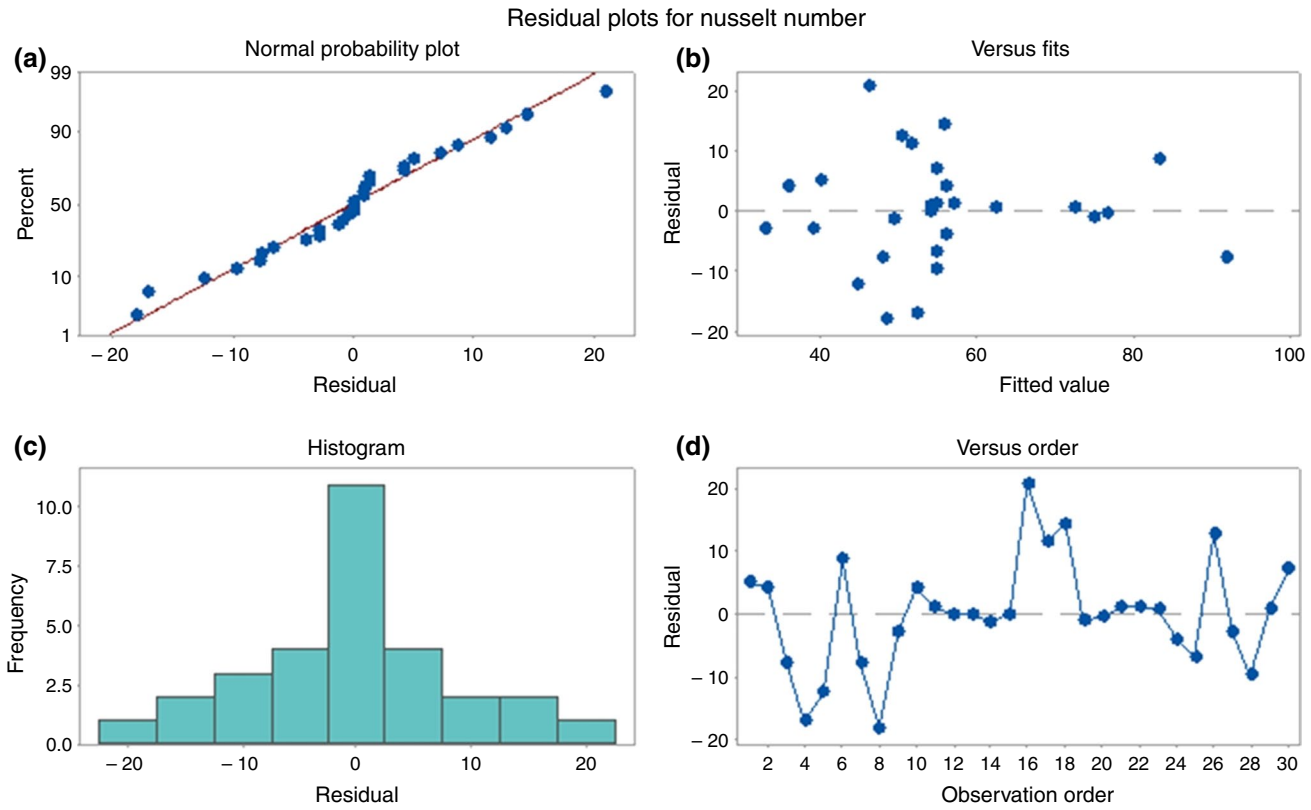


Fig. 25 The residuals chart of the Nusselt number calculations; **a** residuals repetition; **b** residuals normal probability; **c** residuals versus fitted values; **d** the test order-based residuals

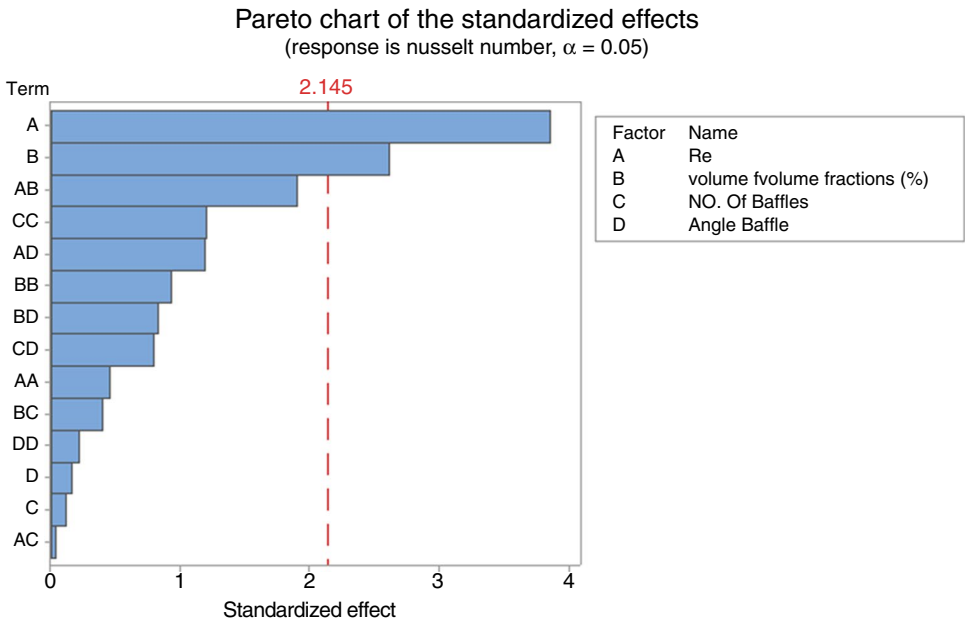


Fig. 26 The efficiency of parameters based on their degree of importance with a $\alpha = 0.05$ value

According to Table 6, it could be concluded that Nusselt number was predicted using triangular baffles based on the response surface method. As it could be observed in the table, the model was reliable enough in order to be applied to the evaluation of fitness of model and model analysis. Also, SS parameter was the sum of squares of the difference between the total average and amount of changes, while the mean squares divided by the degree of freedom derived MS parameter. The F value indicated a comparison between the mean squares and residuals mean square. The P value indicated the probability of observing F value, which confirmed the accuracy of null hypothesis. The lower probability values were specific to the null hypothesis. The P value was compared with a $\alpha = 0.05$ value. Due to the fact that P was a factor higher than 0.05, it could be concluded that its effect on the process was negligible. Therefore, it indicated $a > 0.1$ P value associated with an insignificant effect. It was found that F was determined to be 2.14, which possessed an appropriate compliance model. The high ratio of F, low P, and lack of fitness indicated the fact that the model was not associated with appropriate fitness. Results achieved from the second-order model showed that it was statistically significant, as it was noted in the table with a small P value.

The values achieved for the coefficient of correlation and MSE related to the training, validation, testing, and total data are shown by Fig. 28. The coefficient of correlation was almost 1 for training data, while the MSE value of training, validation, and testing, as well as total data, was, respectively, determined to be 2, 8–9, and almost 4. Results achieved from Perceptron neural network output and experimental data with the number of samples are compared in

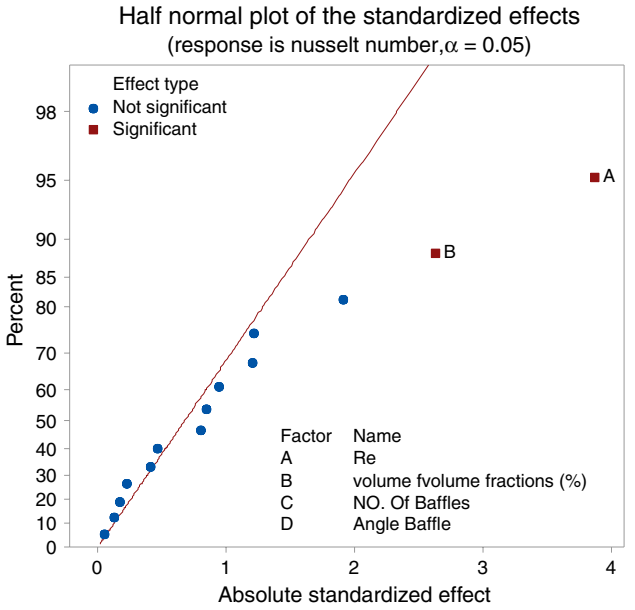


Fig. 27 The efficiency of parameters based on their degree of importance with a $\alpha = 0.05$ value

Fig. 29. The output of neural network for Nusselt number was in a good accordance with experimental data.

The maximum and minimum error values against the number of samples are shown in Fig. 30. The error values close to the base line or zero error led to a more accurate prediction. The maximum tolerance of errors was related to 10–20, 70–80, and 130 samples with a ± 6 error range, while it was found to be ± 2 for other samples.

Table 6 Analysis results and the variance achieved for Nusselt number

Source	DF	Adj SS	Adj MS	F value	*P* value
Model	15	5069.05	337.94	2.14	0.081
Blocks	1	1.84	1.84	0.01	0.916
Linear	4	3502.57	875.64	5.55	0.007
Re	1	2358.16	2358.16	14.94	0.002
Volume fractions (%)	1	1084.90	1084.90	6.87	0.020
No. of baffles	1	2.05	2.05	0.01	0.911
Angle of baffle	1	4.10	4.10	0.03	0.874
Square	4	351.39	87.85	0.56	0.698
Re*Re	1	33.42	33.42	0.21	0.652
Volume fractions (%)*volume fractions (%)	1	138.55	138.55	0.88	0.365
No. of baffles*no. of baffles	1	228.58	228.58	1.45	0.249
Angle of baffle*angle of baffle	1	7.32	7.32	0.05	0.833
2-Way interaction	6	1036.50	172.75	1.09	0.412
Re*volume fractions (%)	1	576.00	576.00	3.65	0.077
Re*no. of baffles	1	0.25	0.25	0.00	0.969
Re*angle of baffle	1	225.00	225.00	1.43	0.252
Volume fractions (%)*no. of baffles	1	25.00	25.00	0.16	0.697
Volume fractions (%)*angle of baffle	1	110.25	110.25	0.70	0.417
No. of baffles*angle of baffle	1	100.00	100.00	0.63	0.439
Error	14	2209.25	157.80		
Lack-of-fit	8	2029.75	253.72	8.48	0.009
Pure error	6	179.50	29.92		
Total	29	7278.30			

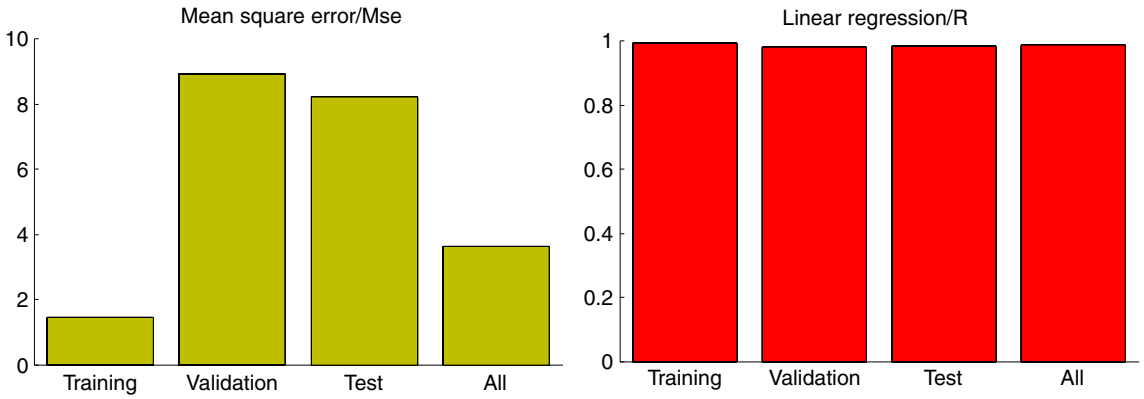


Fig. 28 ANN-derived values of the coefficient of correlation and MSE for Nusselt number

The MSE chart based on repetition steps against the period numbers applied to the processes of training, validation, and experimental dataset of the Nanofluids Nusselt number and triangular baffles is shown in Fig. 31. According to the figure, the number of repetition epochs indicated the fact that the process of predicting Nusselt number would be more successful due to the extension of epochs by the fourth repetition. Moreover, the mentioned enhancement could lead the validation data to be closer to the normal line, which indicated the more accurate prediction. Considering 10 epochs, the effectiveness achieved for the network was determined to be 8.9352. The maximum reduction was achieved for the train data, which was associated with the maximum MSE reduction. Figure 32 shows a diagram design of error distribution related to Nusselt number data. The X values represented the error difference between the achieved experimental values and experimental data, as well as the minimum and maximum errors of the analyte in the chart. Also, the number of samples allocated to the training, validation, and testing sections could be observed on the Y axis. The

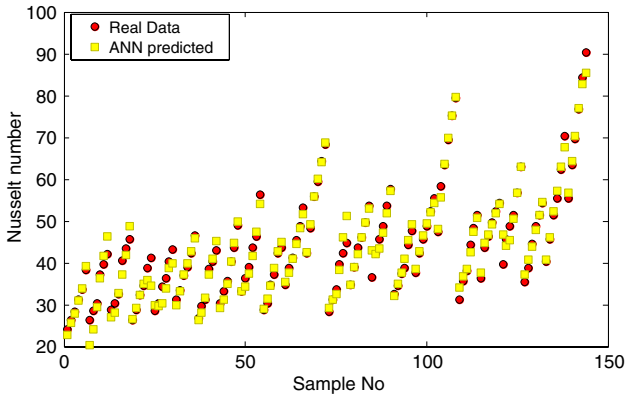


Fig. 29 ANN-predicted and experimental values for Nusselt number based on the samples quantity

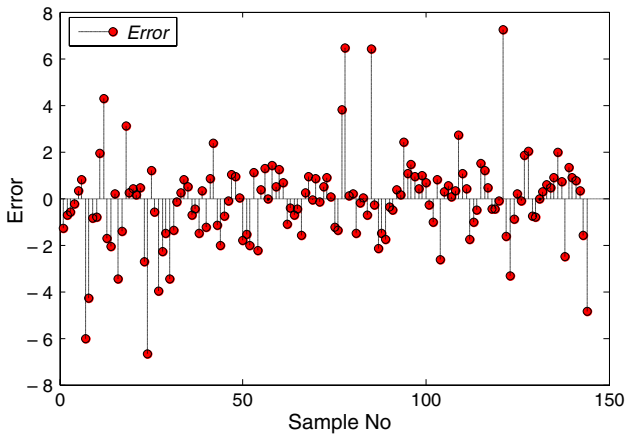


Fig. 30 The upper and lower range of error changes based on the samples quantity

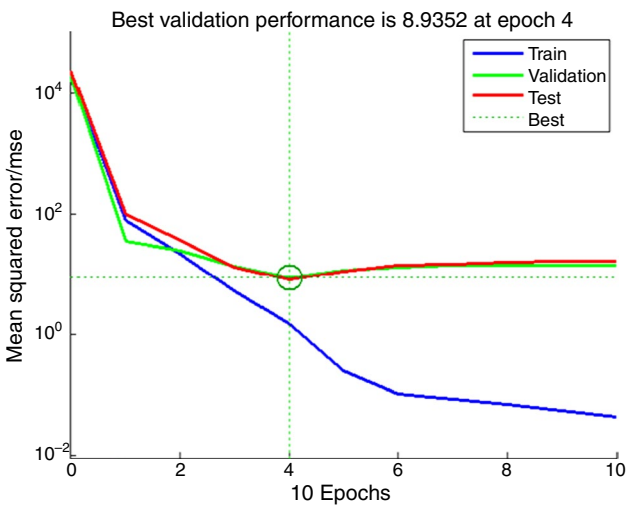


Fig. 31 MSE of the experimental data for Nusselt number (sum of squares-based quantity of repetitions)

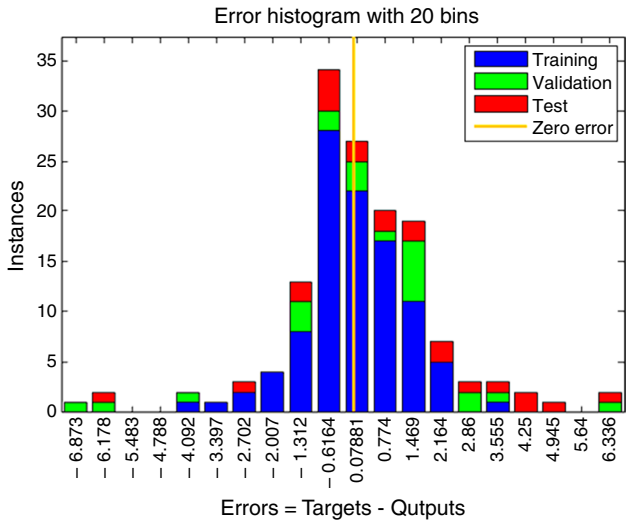


Fig. 32 Error distribution chart for resulted data

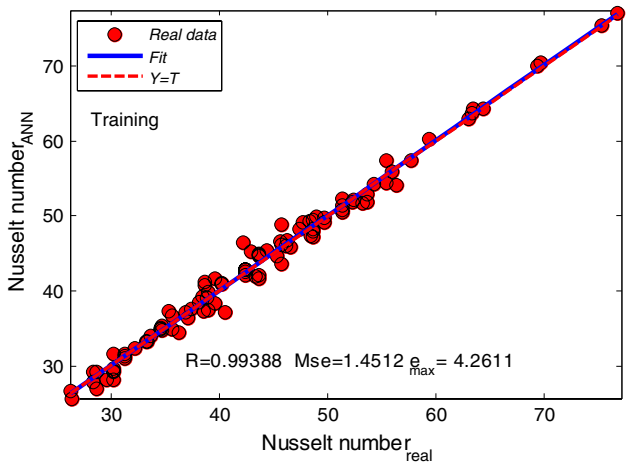


Fig. 33 Coefficient of correlation and MSE values achieved for the experimental and predicted data of Nusselt number with 32 neurons for train data

maximum error values were in the range of ± 4 and mainly included the train data.

According to the regression analysis and coefficient of correlation, there was a linear relationship between the response variable and a number of descriptive variables. The parameters of a linear model were estimated using an objective function. Generally, the linear regression of a linear relationship was considered to be on the basis of the model parameters. The evaluation of values predicted for Nusselt number was carried out using MSE, coefficient of correlation, and maximum error. These values were proposed for training, validation, and total data (Figs.33– 36). The coefficients of correlation were, respectively, determined to be 0.99388, 0.97998, 0.9831, and 0.98828. MSE values were 1.4512, 8.9352, 8.2117,

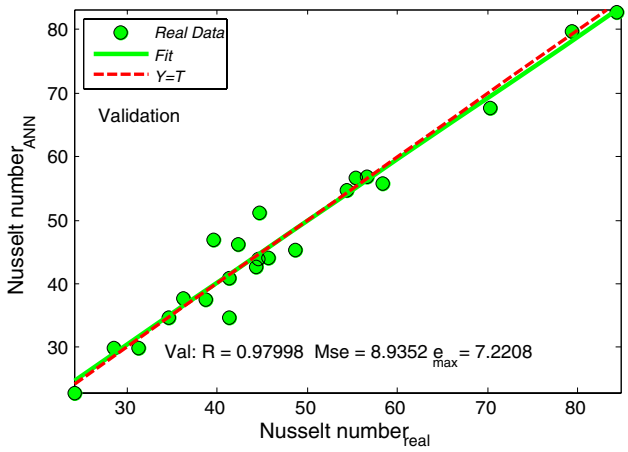


Fig. 34 Values of the coefficient of correlation and MSE value achieved for the experimental and predicted data of Nusselt number with 32 neurons for validation data

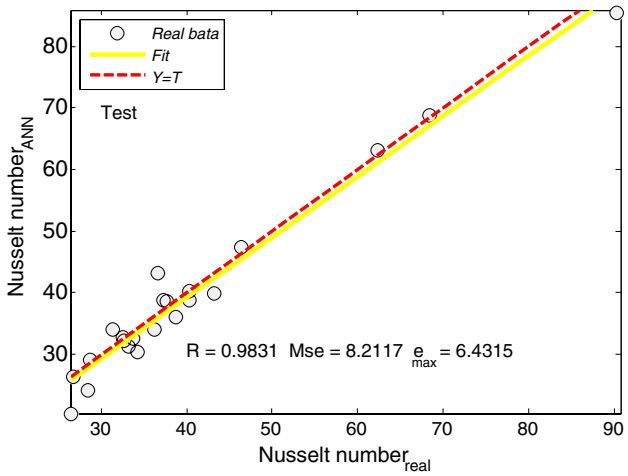


Fig. 35 Values of the coefficient of correlation and MSE value achieved for the experimental and predicted data of Nusselt number with 32 neurons for test data

and 3.6275, respectively. The achieved maximum error values were also determined to be 4.2611, 7.2208, 6.4315, and 7.2208. The regression plan of proposed neural network and data achieved for the coefficient of correlation are shown in Figs. 33– 36. As it could be observed, the figures followed $Y = X$ line and indicated the fact that the network could predict Nusselt number accurately. In other words, a $\cong 1$ coefficient of correlation was required to validate the data correlation.

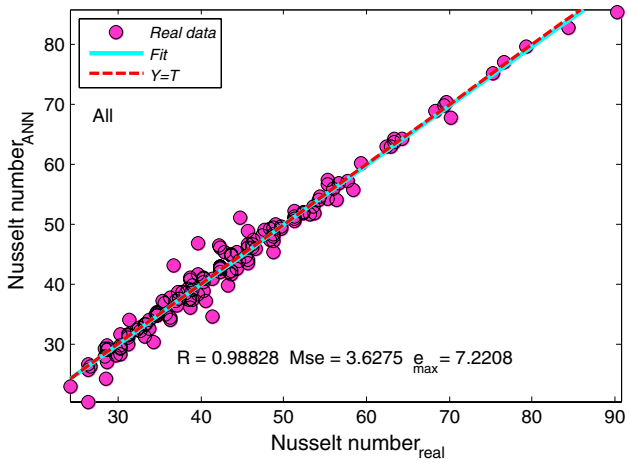


Fig. 36 Values of the coefficient of correlation and MSE value achieved for the experimental and predicted data of Nusselt number with 32 neurons for the total data

Conclusions

In the current study, carbon/water Nanofluid and triangular baffles were applied to a mini-heat exchanger under different angular and numerical conditions. Eventually, the experimental data were evaluated using the response surface method and ANNs with various topologies. The following results were achieved:

1. The extension of Nanofluid volume fraction from 0.1 to 0.3 led to an almost 10% enhancement of coefficient of thermal conductivity and viscosity compared to that of water base fluid. Finally, this led to the increased heat transfer.
2. As a result of increasing the triangular baffles from 4 to 12 and decreasing the baffle angle from 70° to 40°, the velocity of carbon/water Nanofluid was raised around the baffles. Consequently, the heat transfer and Nusselt number increased. The enhancement of triangular baffles quantity also extended the average of coefficient of performance by 15% and 20%, respectively.
3. At moderate Reynolds numbers, it was found that the Nusselt number related to the heat exchangers inner tube with 12 triangular baffles at a 40° angle was determined to be > 8, which was higher than that of the tube with 4 triangular baffles at 70° and 40° angles. The embedment of triangular baffles in the flow path led to a synergy formation between the momentum and heat transfer phenomena and, eventually, Nusselt number extension.
4. The enhancement of Nanofluid concentration from 0.1 to 0.3 increased the related pressure drop and, consequently, coefficient of friction.

5. Results of the response surface method implied the independency of data and residuals. The data distribution was close to the transversal line, which indicated the fact that errors possessed a normal distribution and the fitted model quality was appropriate.
6. Applying 1-32-4 topology to ANN using Levenberg–Marquardt algorithm derived the most adequate prediction of Nusselt number, as the coefficients of correlation were, respectively, determined to be 0.99388, 0.97998, 0.9831, and 0.98828. Moreover, MSE values were found to be 1.4512, 8.9352, 8.2117, and 3.6275. The maximum error values were also 4.2611, 7.2208, 6.4315, and 7.2208.

References

1. Kumar R, Kumar A, Sharma A, Chauhan R, Sethi M. Experimental study of heat transfer enhancement in a rectangular duct distributed by multi V-perforated baffle of different relative baffle width. Heat Mass Transf. 2017;53:1289–304.
2. Ghobadi B, Kowsary F, Veysi F. The influence of geometric parameters of baffle on the flow and heat transfer of Al_2O_3/water nanofluid in a tube with rectangular baffle. Int Nano Lett. 2021;11:395–404.
3. Wang WH, Cheng DL, Liu T, Liu YH. Performance comparison for oil-water heat transfer of circumferential overlap trisection helical baffle heat exchanger. J Central South Univ. 2016;23:2720–7.
4. Ghobadi B, Kowsary F, Veysi F. Heat transfer enhancement using rectangular and triangular shaped baffles with and without nanofluid: new insight into optimization of flow geometric parameters. Prot Met Phys Chem Surf. 2022;58(3):486–500.
5. Hazbehian M, Maddah H, Mohammadiun H, Alizadeh M. Experimental investigation of heat transfer augmentation inside double pipe heat exchanger equipped with reduced width twisted tapes inserts using polymeric nanofluid. Heat Mass Transf. 2016;52:2515–29.
6. Ghasemi N, Aghayari R, Maddah H. Optimizing the parameters of heat transmission in a small heat exchanger with spiral tapes cut as triangles and aluminum oxide nanofluid using central composite design method. Heat Mass Transf. 2018;54:2113–30.
7. Ghazvini M, Maddah H, Peymanfar R, Ahmadi MH, Kumar R. Experimental evaluation and artificial neural network modeling of thermal conductivity of water based nanofluid containing magnetic copper nanoparticles. Phys A. 2020;551:124127.
8. Maddah H, Ghazvini M, Ahmadi MH. Predicting the efficiency of CuO/water nanofluid in heat pipe heat exchanger using neural network. Int Commun Heat Mass Transfer. 2019;104:33–40.
9. Ghasemi N, Maddah H, Mohebbi M, Aghayari R, Rohani S. Proposing a method for combining monitored multilayered perceptron (MLP) and self-organizing map (SOM) neural networks in prediction of heat transfer parameters in a double pipe heat exchanger with nanofluid. Heat Mass Transf. 2019;55:2261–76.
10. Kumaresan G, Santosh R, Duraisamy P, Venkatesan R, Kumar NS. Numerical analysis of baffle cut on shell side heat exchanger performance with inclined baffles. Heat Transfer Eng. 2018;39(13–14):1156–65.
11. Zhang X, Han D, He W, Yue C, Pu W. Numerical simulation on a novel shell-and-tube heat exchanger with screw cinquefoil orifice baffles. Adv Mech Eng. 2017;9(8):1687814017717665.
12. Xiao Q, Yang N, Zhao Z, Dai C, Wu J, Bai F, Tao M (2016) 3-D Numerical simulation of the vapor-liquid flow at the shell side of shell-and-tube heat exchangers. Paper presented at the 2016 24th international conference on nuclear engineering
13. El Maakoul A, Laknizi A, Saadeddine S, Abdellah AB, Meziane M, El Metoui M. Numerical design and investigation of heat transfer enhancement and performance for an annulus with continuous helical baffles in a double-pipe heat exchanger. Energy Convers Manag. 2017;133:76–86.
14. Rao JBB, Raju VR. Numerical and heat transfer analysis of shell and tube heat exchanger with circular and elliptical tubes. Int J Mech Mater Eng. 2016;11:1–18.
15. Wongcharee K, Eiamsa-ard S. Heat transfer enhancement by using CuO/water nanofluid in corrugated tube equipped with twisted tape. Int Commun Heat Mass Transfer. 2012;39(2):251–7.
16. Rosta Abkenar A, Mohhades Deylami H, Dolati F. Experimental investigation of flow and heat transfer in a smooth channel affected by vortex generator with a punched hole. Amirkabir J Mech Eng. 2018;50(2):271–84.
17. Sheikhzadeh GA, Barzoki FN, Arani AAA, Pourfattah F. Wings shape effect on behavior of hybrid nanofluid inside a channel having vortex generator. Heat Mass Transf. 2019;55:1969–83.
18. Han H, Wang S, Sun L, Li Y, Wang S. Numerical study of thermal and flow characteristics for a fin-and-tube heat exchanger with arc winglet type vortex generators. Int J Refrig. 2019;98:61–9.
19. Abdollahi A, Shams M. Optimization of shape and angle of attack of winglet vortex generator in a rectangular channel for heat transfer enhancement. Appl Therm Eng. 2015;81:376–87.
20. Murthy HS, Hegde RN. Heat transfer studies on double tube heat exchanger with combined effect of propeller insert and water-based go and Al_2O_3 nanofluids. Sādhanā. 2022;47(3):143.
21. Promvonge P, Eiamsa-ard S, Wongcharee K, Chuwattanakul V, Samruaisin P, Chokphoemphun S, Eiamsa-ard P. Characterization of heat transfer and artificial neural networks prediction on overall performance index of a channel installed with arc-shaped baffle turbulators. Case Stud Therm Eng. 2021;26:101067.
22. Yaningsih I, Wijayanta AT, Miyazaki T, Koyama S. Thermal hydraulic characteristics of turbulent single-phase flow in an enhanced tube using louvered strip insert with various slant angles. Int J Therm Sci. 2018;134:355–62.
23. Rashidi MM, Nazari MA, Mahariq I, Assad MEH, Ali ME, Almuzaiqer R. Thermophysical properties of hybrid nanofluids and the proposed models: an updated comprehensive study. Nanomaterials. 2021;11(11):3084.
24. Ghalandari M, Irandoost Shahrestani M, Maleki A, Safdari Shadloo M, El Haj Assad M. Applications of intelligent methods in various types of heat exchangers: a review. J Therm Anal Calorim. 2021. https://doi.org/10.1007/s10973-020-10425-3.
25. Kuosa M, Aalto M, Assad MEH, Mäkilä T, Lampinen M, Lahdelma R. Study of a district heating system with the ring network technology and plate heat exchangers in a consumer substation. Energy Build. 2014;80:276–89.
26. Maleki A, Elahi M, Assad MEH, Alhuyi Nazari M, Safdari Shadloo M, Nabipour N. Thermal conductivity modeling of nanofluids with ZnO particles by using approaches based on artificial neural network and MARS. J Therm Anal Calorim. 2021;143:4261–72.
27. Basit Shafiq M, Allauddin U, Qaisrani MA, Rehman TU, Ahmed N, Usman Mushtaq M, Ali HM. Thermal performance enhancement of shell and helical coil heat exchanger using MWCNTs/water nanofluid. J Therm Anal Calorim. 2022;147(21):12111–26.
28. Mazdak S, Sheikhzadeh GA, Fattahi A. Numerical analysis of a heat exchanger with curved segmental baffle and Cassini oval cross-section tubes in various bundle arrangements. J Therm Anal Calorim. 2023. https://doi.org/10.1007/s10973-023-12062-y.

29. Samruaisin P, Maza R, Thianpong C, Chuwattanakul V, Maruyama N, Hirota M, Eiamsa-ard S. Enhanced heat transfer of a heat exchanger tube installed with V-shaped delta-wing baffle turbulators. Energies. 2023;16(13):5237.
30. Dhumal GS, Havaldar SN. Enhancing heat transfer performance in a double tube heat exchanger: experimental study with twisted and helical tapes. Case Stud Therm Eng. 2023;51:103613.
31. Akalin GO, Oztuna Taner O, Taner T. The preparation, characterization and antibacterial properties of chitosan/pectin silver nanoparticle films. Polym Bull. 2022;79(6):3495–512.
32. Oztuna Taner O, Ekici L, Akyuz L. CMC-based edible coating composite films from Brewer's spent grain waste: a novel approach for the fresh strawberry package. Polym Bull. 2023;80(8):9033–58.
33. Dalkiliç AS. A review of flow boiling in mini and microchannel for enhanced geometries. J Therm Eng. 2018;4(3):2037–74.
34. Dalkilic AS. Parametric study of energy, exergy and thermoeconomic analyses on vapor-compression system cascaded with libr/water and nh3/water absorbtion cascade refrigeration cycle. Anadolu Univ J Sci Technol A-Appl Sci Eng. 2017;18(1):78–96.
35. Gnielinski V. New equations for heat and mass transfer in turbulent pipe and channel flow. Int Chem Eng. 1976;16(2):359–67.
36. Petukhov BS. Heat transfer and friction in turbulent pipe flow with variable physical properties. Adv Heat Transfer. 1970;6:503–64.

Publisher's Note Springer Nature remains neutral with regard to jurisdictional claims in published maps and institutional affiliations.

Springer Nature or its licensor (e.g. a society or other partner) holds exclusive rights to this article under a publishing agreement with the author(s) or other rightsholder(s); author self-archiving of the accepted manuscript version of this article is solely governed by the terms of such publishing agreement and applicable law.